

Refinement of Monocular Depth Maps via Multi-View Differentiable Rendering

Laura Fink^{1,2}

Linus Franke¹

Joachim Keinert²

Marc Stamminger¹

¹Friedrich-Alexander-Universität
Erlangen-Nürnberg
{first.last}@fau.de

²Fraunhofer IIS
Erlangen
{first.last}@iis.fraunhofer.de

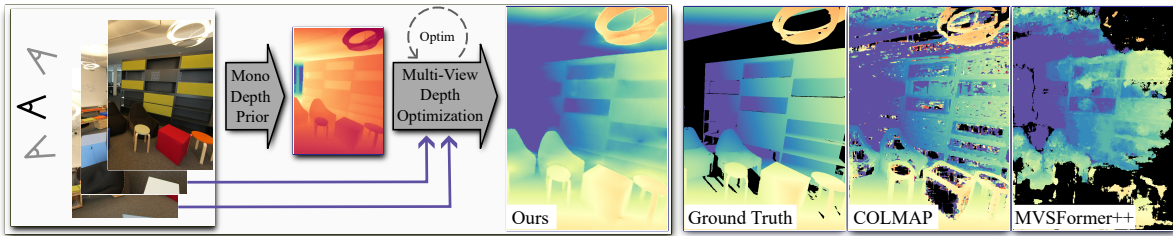


Figure 1. Our novel algorithm refines a depth map from a monocular estimator with multi-view differentiable rendering based on a meshed representation of the target depth map. This results in dense and accurate depth maps, especially in challenging indoor scenarios. Note that the ground truth here is obtained from a meshed LiDAR scan, as such uncertain areas are left blank.

Abstract

The accurate reconstruction of per-pixel depth for an image is vital for many tasks in computer graphics, computer vision, and robotics. In this paper, we present a novel approach to generate view consistent and detailed depth maps from a number of posed images. We leverage advances in monocular depth estimation, which generate topologically complete, but metrically inaccurate depth maps and refine them in a two-stage optimization process based on a differentiable renderer. Taking the monocular depth map as input, we first scale this map to absolute distances based on structure-from-motion and transform the depths to a triangle surface mesh. We then refine this depth mesh in a local optimization, enforcing photometric and geometric consistency.

Our evaluation shows that our method is able to generate dense, detailed, high-quality depth maps, also in challenging indoor scenarios, and outperforms state-of-the-art depth reconstruction approaches. Overview and supplemental material of this project can be found at https://lorafib.github.io/ref_depth/.

1. Introduction

Depth estimation plays a fundamental role in various fields of computer vision, graphics, and robotics. It is a criti-

cal component for tasks such as scene understanding, object recognition, navigation, and 3D reconstruction. Accurate depth information enable applications like autonomous driving, augmented reality, robot navigation, and virtual scene exploration via image-based rendering.

Depth maps are images with a depth value per pixel. Active sensors such as LiDAR [28] or Time-of-Flight cameras [70, 71] can measure such maps directly. Alternatively, depth maps can be reconstructed from images by image-to-image patch matching (stereo cameras [43] or multi-view stereo [1, 16]). Thus generated depth maps are often incomplete, exhibit low resolution, or are not pixel-wise aligned with input images, which imposes problems on many tasks that assume pixel-precise multi-view consistency.

In recent years, these techniques were elevated by deep learning, which made it possible to find efficient heuristics or helped to densify sparse depth information [13, 32, 53, 65, 75]. Mono image depth estimation methods [12, 21, 63, 64] go one step further and estimate depth maps from a single given image directly, using strongly pre-trained networks. These approaches show impressive results, capturing surface structures and depth topology with high detail. However, the generated depth maps are usually in a normalized, non-metric range, or their absolute depth is too imprecise for many tasks, where multi-view consistency is required, like e.g. image-based rendering.

In this paper we present a novel method to acquire de-

tailed, dense, absolute, and multi-view consistent depth maps based on a series of posed input images. Our pipeline works as follows: First, we estimate per-image depths with strongly pretrained mono-depth estimation techniques [21], yielding topologically smooth depth maps, which still lack metrically correct distances. After converting this depth map to a triangle mesh, we optimize the depth mesh towards a finely detailed multi-view consistent depth map with absolute distances using a differentiable renderer [26]. The optimization happens in two stages. First, we learn a neural field that remaps initial depth values coarsely to correct values, taking also into account a sparse 3D reconstruction. Second, we apply local depth map refinement yielding highly detailed, multi-view consistent results.

As we show in our evaluation on synthetic and real-world data, our method provides highly detailed and accurate depth maps, surpassing competing methods in accuracy. Our contributions are:

- A novel analysis-by-synthesis technique to refine mono depth maps for accurate 3D information via view consistency optimization.
- A two step refinement scheme that first performs a coarse alignment via shallow neural fields and second follows a local refinement strategy to optimize depth values on fine granularity for highly detailed depth maps.
- Effective edge aware and poisson blending [37] inspired regularizers to exploit the strong initial estimates from mono estimators.
- An extensive evaluation of the proposed method, showcasing its efficiency especially on challenging feature-scarce indoor scenes.

The source code is available at

https://github.com/lorafib/ref_depth/.

2. Related Work

In this section, we provide an overview on the various ways to measure or estimate depth information, often in the form of (preferably dense) depth maps, and also discuss ways to refine these acquired information.

Active Sensing. Depth can be measured using active systems which send some form of light pulses and observe their reflection, thus deducing the distance to the sensor. Structured light systems [39, 71] project different light patterns onto an object and estimate depth from the deformation. These systems are very accurate at close range and in controlled environments. However, they are sensitive to external lighting conditions making them unsuitable for many in-the-wild applications. Other active depth sensors are LiDAR [28, 51] or time-of-flight cameras [70, 71]. These systems send pulses of light and measure the elapsed time until their reflections impinge the sensor, thus, deducing the

distance the light must have been traveled. However, resulting depth maps are often low resolution and struggle with glossy materials.

Image-based Matching & Triangulation. Another well known option are stereo cameras [22, 43], where image patches are matched and triangulated based on the patches' horizontal disparity [1]. As their baseline is fixed, their depth range with optimal accuracy is limited.

Multi-view-stereo (MVS) [16, 41] techniques expand this paradigm by considering information from two or more images. Similar to patch-based correspondence finding in stereo pairs, image patches are compared along the epipolar line and the likelihood of the match is maximized by calculating the patches' similarity. Texture scarce regions are challenging for matching, often leading to sparse depth maps in such ambiguous regions. To compensate for this, coarse-to-fine approaches [54, 58] or plane prior assistance got established [54, 59, 69].

Alternatively to patch matching, another common algorithm for MVS depth estimation is the plane-sweep algorithm [8]. Plane sweeping describes the process of discretizing the viewing volume into fronto-parallel planes at hypothetical depths and warping (sweeping) them into other views. Thus, the color information of all available views are backprojected to the volume bounded by the camera frustum. Eventually, the depth hypothesis is chosen that maximizes photometric consistency. As this process involves a volumetric representation of the scene, the memory consumption can be quite high.

Neural methods. Yao et al. [65] elevated the plane sweep approach into the deep learning era. Several follow up works refined the initial architecture and training, using attention modules [9, 30, 31] or coarse-to-fine schemes [4, 14, 62]. To find the best fitting depth hypotheses, the so-called cost volume, which contains all the hypotheses, is processed by another network. This can be e.g. a recurrent neural network [55, 60, 66] or a 3D CNN [75]. To this date, these networks dominate popular benchmarks like the Tanks and Temples [25] point cloud reconstruction benchmark [7]. More recently, vision transformers were successfully incorporated into these types of network architecture [3, 5], which enhance performance for feature extraction significantly.

Novel View Synthesis & Inverse Rendering. In the realm of novel view synthesis (NVS), depth maps serve as a common way to represent an underlying 3D scene which is used to create novel views [10, 17]. Thus, some methods started to produce depth maps within their pipeline more or less as byproduct to enable high quality NVS [52, 56, 73].

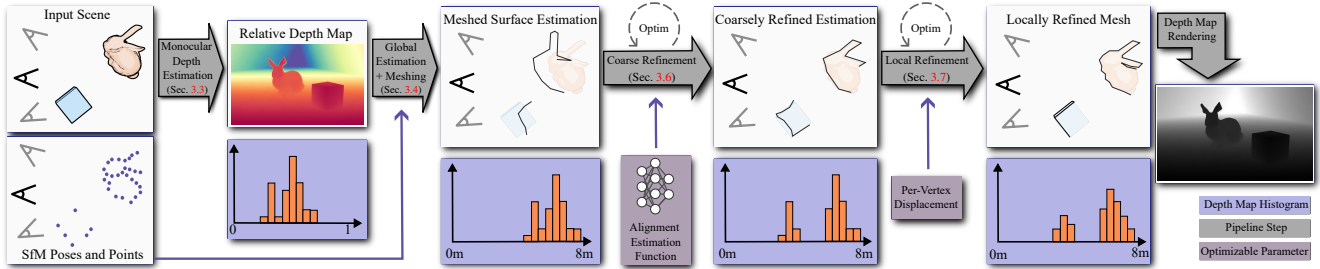


Figure 2. Overview of our method: We employ monocular depth estimation for a relative, but topologically complete depth map. Results from Structure-from-Motion are used to scale the depth map to absolute space. Following, we convert the depth map to a surface mesh for refinement via differentiable rendering. The refinement is done in two consecutive steps: first, we learn a mapping function that smoothly aligns the depth map to the sparse point cloud and second, we refine per-vertex positions.

However, these depth maps often have very limited depth precision [56] or resolution [52].

Others use advancements from the novel view synthesis and inverse rendering community to directly optimize for depth maps. Kim et al. [23] integrate image-based rendering methods [29] to infer view-consistent depth maps. Chugunov et al. [6] transfer multi resolution hash grids as proposed by Müller et al. [34] to optimize near-field depth maps from RAW camera bursts supported by sensor data like acceleration and angular velocity. Mirdehghan et al. [33] and Shandilya et al. [42] cast structured-light scanning as an inverse rendering problem to achieve high quality depth information.

Refinement. To address the shortcomings observed in depth maps, such as sparseness and noise, many approaches focus on refining low-quality depth maps using auxiliary information or by fusing data from other sensors, such as registered photographs. Shape-from-shading-based techniques estimate curvature from the observed light-surface-interaction, leveraging registered color information to improve depth map quality [15, 20, 35, 36, 49, 57]. Others try to optimize for photometric consistency across views. For instance, Ito et al. [19] aim to densify sparse 3D information from MVS depth maps by leveraging photometric consistency. This allows to fill in missing data using a NeRF-based optimization scheme.

Other methods [13, 32, 72] use neural networks to complete depth maps from sparse data like LiDAR point clouds. Similarly, low-resolution depth maps are upsampled using shape-from-shading [15] or temporal information [47, 68]. Other approaches tackle noise [44, 61] in depth maps, which becomes particularly severe at greater distances, as noise scales non-linearly for sensors like time-of-flight cameras and stereo cameras with fixed baselines suffer from diminishing disparities.

Monocular Depth Estimation Monocular depth estimators [21, 63, 64] take shading-based refinement and image-

based depth densification even further by inferring 3D structures from a single image. They try to mimic human scene understanding by using heuristics related to object sizes, focus, and light interaction. Extensive training data has turned these estimators into highly effective color-based filters for scene comprehension.

Despite monocular depth estimators being geometrically inaccurate [12] and ambiguous due to their lack of geometric triangulation, they excel at providing priors for 3D scene understanding. Many methods already deliver depth maps with pixel-perfect silhouettes and close approximations of curvatures. Unsurprisingly, these estimators were successfully integrated to multi-view systems [23] or for regularization of related tasks such as NVS [27].

3. Method

3.1. Overview

We aim to build a pipeline which provides highly detailed and multi-view consistent depth maps for a set of posed input images. Given are $n + 1$ input images $\mathbf{I}_i \in \mathbb{R}^{H \times W \times 3}$, $i \in \{0, \dots, n\}$, with W and H being the images width and height. Furthermore given is a sparse 3D reconstruction from these images, delivering poses for all images and a sparse point cloud. In this section, we describe how to compute a particular depth image $\mathbf{D}_0 \in \mathbb{R}^{H \times W \times 1}$ for input image \mathbf{I}_0 by taking into account all other input images. Also see Fig. 2 for a visualization.

The overall idea is to start with a *relative* depth map \mathbf{D}_0^r , obtained by monocular depth estimation. If the depth estimator is not metric (as most are), we coarsely scale to absolute (*global*) values using the depth values of the point cloud (see Sec. 3.2), obtaining \mathbf{D}_0^g . The resulting map is detailed, but metrically incorrect or at least very approximate, yet their relative depths are more reliable and well aligned with the RGB images they were obtained from.

\mathbf{D}_0^g is then converted to a depth mesh \mathbf{M}^g with small triangles, which is used for further optimization. Using such a depth mesh instead of a depth image eases optimization via

inverse rendering, and additionally serves as a regularization for further optimization. We can also use mesh reduction in between to further regularize our results and lower resource consumption. Furthermore, some applications like image-based rendering, can directly work on the resulting depth mesh.

The initial depth mesh \mathbf{M}^g with crude depth values is then optimized in two steps: First, we do a *coarse refinement* via a shallow coordinate MLP, producing an improved depth mesh \mathbf{M}^c (see Sec. 3.6). This step mostly aligns the depth mesh with the sparse point cloud (see Tab. 4).

In the second optimization, we *locally* refine (see Sec. 3.7) the depth mesh using differentiable rendering aiming for photo-consistency with the other images, resulting in a well aligned, view consistent, and precise depth mesh.

3.2. Input

We first use Structure from Motion, more precisely COLMAP [40], to estimate intrinsics C_i and pose $\{(R, t)_i\}$ of each image, as well as a sparse point cloud $\mathbf{X} = \{x_j\}$ with all x_j being visible in \mathbf{I}_0 . C is defined with the common convention of focal lengths (f_x, f_y) and principal point (c_x, c_y) and images are undistorted.

3.3. Mono Depth and Global Estimation

We estimate a depth map \mathbf{D}_0^r for \mathbf{I}_0 using a strongly pre-trained monocular depth estimator [21]. To approximately map the relative depth map \mathbf{D}_0^r to an absolute scale, we use the sparse point cloud \mathbf{X} : we globally (g) offset and scale \mathbf{D}_0^r such that its median distance and the value of its 0.1th percentile are aligned with the corresponding values of the sparse point cloud \mathbf{X} , resulting in depth image \mathbf{D}_0^g .

3.4. Meshing

Next, we convert \mathbf{D}_0^g to a 3D depth mesh \mathbf{M}^g . We opted for a meshed representation as it allows for a non-uniform representation of the underlying geometry. Furthermore, depth maps are a 2.5D scene representation making it intuitive which regions belong to a common scene element as they are often separated by obvious discontinuities. A meshed representation will preserve geometric continuity and will prevent outliers or noise which would lead to isolated or disconnected points, as often observed for pixel-wise depth estimations.

Triangle mesh. We unproject depth samples at image position (u, v) with $u \in [0, W - 1]$ and $v \in [0, H - 1]$ to obtain a vertex $p = (x, y, z)^T$ with

$$x = (u - c_x) \frac{z}{f_x}, \quad y = (v - c_y) \frac{z}{f_y}. \quad (1)$$

and connect the vertices via triangle-based quads.

During this step we downsample the depth image by a factor d , which heavily reduces the number of triangles by a factor d^2 and improves performance. We loose some resolution, but since later optimizations can move (u, v) , we benefit from a better regularization. Furthermore, we avoid sub-pixel sized triangles, which do not receive gradients during differentiable rasterization (see Sec. 3.5).

Colors for the mesh are directly taken from \mathbf{I}_0 according to the interpolated image coordinates (u, v) . Note that this decouples geometric complexity from image resolution and allows further reduction of vertices.

Decimation. As \mathbf{D}_0^g equips us with a very detailed scene topology prior, we can approximate where optimizable parameters are need to be spent before optimization. Hence, we integrate a decimation step within our pipeline, to reduce \mathbf{M}^g 's complexity. This step implicitly regularizes the refinement, as plane-like geometry is represented by fewer primitives and can be seen analogously to plane prior assistance known from patch match-based methods [59]. Fig. 4 highlights this for a very challenging scene with many feature-scarce walls.

In practice, we apply quadric mesh decimation [11] to the unprojected mesh vertices prior to the local refinement (see Sec. 3.7). Decimation of the vertices in non-linear space (see Sec. 4) favors a higher vertex density closer to the camera. This works well with quadric mesh decimation as it does not touch positions, thus no incorrect non-linear interpolation will arise. We keep a ratio r of the original amount of vertices after the decimation (see Sec. 5.2).

3.5. Differentiable Rendering

We use a differentiable render function Φ defined as

$$(\mathbf{I}_i^*, \mathbf{D}_i^*) = \Phi(C_i, R_i, t_i, C_0, R_0, t_0, \mathbf{M}). \quad (2)$$

Φ projects the current mesh \mathbf{M} with camera parameters R_0, t_0, C_0 to a neighboring view i with R_i, t_i, C_i , creating a pair of synthesized RGB images and depth maps. Specifically, all vertices $p \in \mathbf{M}$ are projected with

$$p_i = C_i(R_i|t_i)(R_0|t_0)^{-1}p \quad (3)$$

and then rasterized. p_i^* is

During optimization, the state of \mathbf{M} continuously changes as described in Sec. 3.6 and 3.7. In the following, we denote the current state of the depth map as \mathbf{D}_0^* . Returning from the meshed representation \mathbf{M} to \mathbf{D}_0^* is straight forward by evaluating Φ with C_0, R_0, t_0 , which also yields \mathbf{I}_0^* , both of which are rasterized versions of \mathbf{M} .

3.6. Coarse Refinement

In the first optimization stage, the goal is to transfer the initial depth estimation \mathbf{D}_0^g to more accurate values. Note

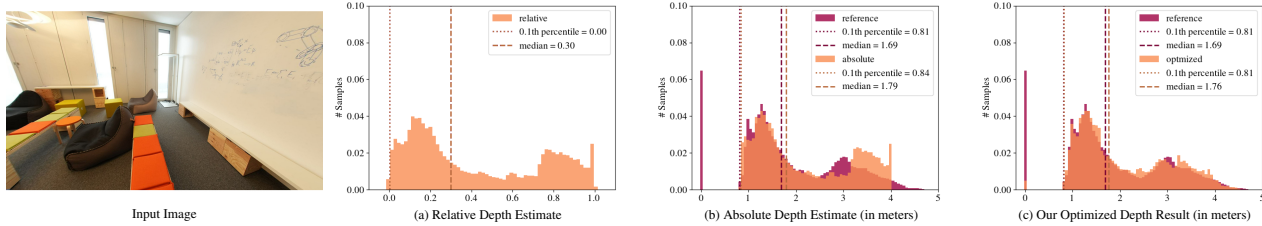


Figure 3. Histograms of different states of depth maps during our optimization. The initial estimate (a) is in relative space and taken as input to be refined (orange). Our absolute estimation (b) brings this to absolute space, which we then optimize (c) to closely capture the depth distribution of the ground truth (red).



Figure 4. Visualization of our depth mesh M . Numbers in lower left corner indicate decimation ratio r . Here, $d = 8$, thus reducing 1738k values of the depth map to 55k vertices. After decimation with $r = 0.5$, 27k vertices, and with $r = 0.25$, 14k vertices are left. In practice, we used $d = 4$ and $r = 0.5$ (see supplemental).

that in this stage, we do not aim for high precision, but to coarsely align our depth buffer.

To this end, we determine a field that yields an offset o and a scale s for any given image coordinate (u, v) , thus mapping depth values $z^g \in \mathbf{D}_0^g$ to refined z^c :

$$z^c = z^g(1 + s^c) + o^c \quad \forall z^g \in \mathbf{D}_0^g, \quad (4)$$

with $(o^c, s^c) = \Psi(u, v, z^g)$,

thus arriving at depth map \mathbf{D}_0^c .

More precisely, the refinement function Ψ is modelled as a shallow multi-layer perceptron (MLP) with positional encoding [48]:

$$(o^c, s^c) = \Psi(\gamma^m(u), \gamma^m(v), \gamma^k(z^g)), \quad (5)$$

where γ^m and γ^k indicate positional encoding functions of degree m and k , respectively.

For optimization of the function, we evaluate Ψ directly at available image positions of the sparse point cloud \mathbf{X} and also compare \mathbf{D}_0^c against \mathbf{X} and use the regularizer as described in Sec. 3.8 using gradient descent. Evaluating the losses of \mathbf{D}_0^c will prevent overfitting of Ψ solely to the available points. The weights of Ψ are initialized very small, thus o^c and s^c will be small and thus z^c close to z^g .

Using a shallow MLP with low frequent positional encoding inherently exploits the spectral bias of MLPs, mapping similar inputs to similar outputs [48]. Hence, the re-

mapped depth map retains smooth image regions as well as discontinuities.

3.7. Local Refinement

The second stage of our refinement aims to finely tune \mathbf{D}_0^c , arriving at \mathbf{D}_0 . Therefore, we jointly optimize depth values z with vertex image coordinates u, v and interject mesh decimation steps in between. The local refinement step aligns the surface mesh with edges in the image and adjusts depth values to finely describe the surface.

Depth Refinement. To efficiently optimize depths, we introduce an inverse scaling factor f_z per vertex which serves as the optimizable parameter.

$$z = \frac{z^c}{f_z} \quad (6)$$

Note that local depth refinement is not optimized during the coarse refinement, but rather started afterwards.

Coordinate Refinement. We further introduce the optimizable image space offsets $\Delta u, \Delta v$ per vertex, thus allowing for a piece-wise linear approximation of silhouettes. $\Delta u, \Delta v$ are applied to the vertices with

$$(u, v) = (u^g + \Delta u, v^g + \Delta v). \quad (7)$$

$\Delta u, \Delta v$ are limited by $\frac{d}{2}$ to ensure that the mesh vertices won't intersect. Note that in contrast to f_z , $\Delta u, \Delta v$ are optimized already during the coarse refinement.

As in the previous refinement, $\Delta u, \Delta v$ and f_z are optimized with gradient descent as Φ is evaluated repeatedly with (C_i, R_i, t_i) and optimized according to the losses described in the following section.

3.8. Losses & Regularizers

In this section, we describe the two losses and three regularizers that are used to control and stabilize our optimization.

Regularizers. For training regularization, we apply three different regularizers.

\mathcal{R}_s is a simple regularizer that suppresses noisy results:

$$\mathcal{R}_s(\mathbf{D}_0^*) = \|\mathbf{D}_0^* - g(\mathbf{D}_0^*)\|_2, \quad (8)$$

where g is a Gaussian blur with window size 5.

The regularizers \mathcal{R}_p and \mathcal{R}_e have the goal to maintain structural information from the mono depth image \mathbf{D}_0^r . To this end, we calculate edge images \mathbf{E}_0^r and \mathbf{E}_0^* from \mathbf{D}_0^r and \mathbf{D}_0^* by utilizing a Sobel filter-based edge detection. The edge images \mathbf{E} have values $\in [-1, 1]$, with values below 0 indicating edges and discontinuities and values above 0 indicating surfaces. Following, we define the edge regularizer \mathcal{R}_e as

$$\mathcal{R}_e(\mathbf{E}_0^*, \mathbf{E}_0^r) = \|\max(0, \mathbf{E}_0^*) - \max(0, \mathbf{E}_0^r)\|_2 + \frac{1}{|\mathbf{M}|} \sum_{j=1}^{|\mathbf{M}|} \mathbf{e}_{u', v'} \quad (9)$$

where $\mathbf{e}_{u', v'}$ are the sampled values of \mathbf{E}_0^r at image coordinates u', v' and $|\mathbf{M}|$ is the amount of vertices present in the mesh \mathbf{M} . The first term of \mathcal{R}_e encourages that silhouettes of \mathbf{D}_0^* and \mathbf{D}_0^r align without enforcing the absolute values to match (thus, clamping the edge images at 0). The second term encourages the offsets $\Delta u, \Delta v$ to move the vertices' image coordinates to the midpoint of the edges.

Inspired by Poisson blending [37], we define \mathcal{R}_p as:

$$\begin{aligned} \mathcal{R}_p(\mathbf{D}_0^*, \mathbf{D}_0^r) = & \|\max(0, \mathbf{E}_0^r)(\nabla_u \tilde{\mathbf{D}}_0^* - \nabla_u \mathbf{D}_0^r)\|_2 + \\ & \|\max(0, \mathbf{E}_0^r)(\nabla_v \tilde{\mathbf{D}}_0^* - \nabla_v \mathbf{D}_0^r)\|_2. \end{aligned} \quad (10)$$

$\tilde{\mathbf{D}}_0^*$ is \mathbf{D}_0^* normalized to $[0, 1]$. ∇_u and ∇_v are the image space gradient operators in u and v direction. For \mathcal{R}_p , we use \mathbf{E}_0^r to mask out silhouettes as we only want to transfer local structural details while preserving absolute scale while neglecting bigger discontinuities, which are prone to be inaccurate.

Geometric Loss. \mathcal{L}_{geo} measures the distance between the current depth buffer and the depth values of the projected sparse point cloud. It is defined as

$$\mathcal{L}_{geo}(\mathbf{D}_0^*, \mathbf{D}_0^c, \mathbf{X}) = l_{geo}(\mathbf{D}_0^*, \mathbf{X}) + l_{geo}(\mathbf{D}_0^c, \mathbf{X}), \text{ with} \quad (11)$$

$$l_{geo}(\mathbf{D}, \mathbf{X}) = \frac{1}{|\mathbf{X}|} \sum_{j=1}^{|\mathbf{X}|} \frac{\mathcal{H}_\delta(z_j^D, z_j^X)}{z_j^X}. \quad (12)$$

\mathcal{H} is the Huber loss [18] with $\delta = 0.5$. $|\mathbf{X}|$ is the number of points available in \mathbf{X} . z_j^X are the available depth values from the sparse point cloud \mathbf{X} , projected to the current view, and z_j^D the corresponding depth values of \mathbf{D}_0^* or \mathbf{D}_0^c , respectively, evaluated at the image space coordinates of \mathbf{X} . $l_{geo}(\mathbf{D}_0^c, \mathbf{X})$ will only come into effect during the coarse refinement.

Photometric Loss We use a standard mean squared error formulation for our photometric consistency loss \mathcal{L}_{photo} between rendered \mathbf{I}_i^* and captured images \mathbf{I}_i :

$$\mathcal{L}_{photo}(\mathbf{I}_i^*, \mathbf{I}_i) = \|\max(0, \mathbf{E}_i^*)(\mathbf{I}_i^* - \mathbf{I}_i)\|_2. \quad (13)$$

$\max(0, \mathbf{E}_i^*)$ indicates the projected depth map \mathbf{E}_i^* will mask out regions of \mathbf{I}_i which were occluded in \mathbf{I}_0 .

Our total evaluation loss combines the introduced objective functions using a weighted sum of each of the elements, see supplemental material.

4. Depth Refinement with GPU Acceleration

Using a GPU hardware accelerated framework for our depth refinement is preferable due to implementation simplicity and optimization speed. This however is challenging as common hardware implementations (e.g. NVDiffRast [26]) follow hardware specifications and use a non-linear, *reciprocal* depth formulation, normalized between $[-1, 1]$ after screen projection. Additionally, this formulation uses a near plane d_{near} and far plane d_{far} which restricts the minimal and maximal length of the camera ray of the principal point resulting in a 4×4 matrix P .

We convert the previously used intrinsics definition C with $\{f_x, f_y, c_x, c_y\}$ to the projection matrix P following the OpenGL convention [2] and using homogeneous 4D coordinates for all vertices. This $P_{\{0..N\}}$ is then used in place of $C_{\{0..N\}}$ in Equ. 3.

Adjusting to this projection scheme and its reciprocal depth formulation for depth refinement however requires several adjustments to our method:

Meshing. The z coordinates of \mathbf{M} are stored in reciprocal space, given by

$$z' = \frac{d_{far} + d_{near}}{d_{near} - d_{far}} + \frac{2d_{far}d_{near}}{-z^g(d_{near} - d_{far})}. \quad (14)$$

u and v are stored in normalized image coordinates in the $[-1, 1]$ range with

$$(u', v') = \left(\frac{2u^g}{W} - 1, \frac{2v^g}{H} - 1 \right) \quad (15)$$

An upside of this normalization is that it improves numerical stability and is also simplifies positional MLP encoding (see Sec. 3.6).

Depth and Vertex Refinement. For both global and local refinement, depth optimization in reciprocal space leads to instable optimization. As such we do this optimization in linear space by evaluating and substitute the rightmost part in Equ. 3 first by

$$p'' = \frac{1 + s_c}{f_z} P_0^{-1}((u' + \Delta u, v' + \Delta v, z', 1)^T + o_c). \quad (16)$$

In this representation, Δu and Δv are now limited by $\frac{j}{W}$ and $\frac{j}{H}$ respectively.

Regarding the depth, we also need to prevent vertices from moving outside the view frustum by

$$p' = \min\left(-\frac{d_{far}-\epsilon}{z}, 1\right) \max\left(-\frac{d_{near}+\epsilon}{z}, 1\right)p'' \quad (17)$$

with ϵ empirically set to 10^{-6} . As such we do depth optimization in linear space while keeping image coordinate optimization in projected space.

Thus, Equ. 3 can be rewritten as:

$$p_i = P_i(R_i|t_i)(R_0|t_0)^{-1}p' \quad (18)$$

with $(R|t)$ matrices now being 4×4 dimensional, respectively.

5. Results

We evaluate our approach on the synthetic Replica dataset [38, 46] and the real-world ScanNet++ dataset [67]. Both data sets provide metric scale ground truths.

For the Replica dataset, color and ground truth depth maps are obtained from the rendered meshes. We selected four scenes, and optimized 64 depth maps for each. As sparse point clouds, we generate point samples from the ground truth meshes and add 2-10% noise as well as outliers to them (see Appendix B for details).

As for the ScanNet++ dataset, ground truth depth maps are rendered from the meshes, the sparse point cloud and poses have been computed by COLMAP [40]. For the results present in Sec. 5.1, we used 10 scenes from the ScanNet++ validation set and 10 depth maps of each (100 in total). Details on the dataset preparations can be found in Appendix B. For hyperparameter tuning, we used 7 different scenes.

Implementation details, the following results were created with, are in the supplements.

5.1. Comparison against Prior Arts

We compare our approach with the top three methods of the Tanks and Temples benchmark at the time [25]. All of them are MVSNet-based methods [65]: MVSFormer [3], MVSFormer++ [5], and GeoMVSNet [74]. For GeoMVSNet however, only weights trained on the DTU dataset were available, which impacted generalization capabilities. These methods produce a certainty value that can be thresholded to control outlier removal and depth map completeness. For comparisons, we considered only depth values with valid ground truth within a 7-meter range, to stay within the specified bounding volumes for related methods, and masked values according to their certainty thresholds of 0, 0.25, and 0.5. The metrics of resulting depth maps, which vary in completeness, are documented in the tables.

Method	Valid Samples	RMSE	MAE	L1-rel	L1-inv	δ_1	Acc. 0.01 m	Acc. 0.05 m	Acc. 0.10 m
MVSFormer (0)	1.00	0.80	0.31	0.13	0.17	0.88	0.21	0.58	0.73
MVSFormer++ (0)	1.00	0.56	0.27	0.10	0.22	0.89	0.23	0.61	0.76
MVSFormer (0.25)	0.97	0.75	0.27	0.11	0.11	0.90	0.21	0.58	0.73
MVSFormer++ (0.25)	0.95	0.42	0.17	0.06	0.08	0.93	0.23	0.61	0.76
MVSFormer (0.5)	0.87	0.46	0.14	0.06	0.03	0.96	0.21	0.57	0.71
MVSFormer++ (0.5)	0.85	0.19	0.07	0.03	0.01	0.98	0.22	0.59	0.73
Ours (+)	0.99	0.08	0.04	0.02	0.01	1.00	0.37	0.81	0.92
Ours (-)	0.99	0.09	0.05	0.02	0.01	0.99	0.26	0.69	0.87

Table 1. Results on the Replica dataset. In brackets are the confidence thresholding for MVSNet-based methods and sparse point cloud accuracy with good (+) and poor (-) quality.

Method	Valid Samples	RMSE	MAE	L1-rel	L1-inv	δ_1	Acc. 0.01 m	Acc. 0.05 m	Acc. 0.10 m
COLMAP	69%	0.60	0.30	0.24	0.49	0.73	0.17	0.35	0.41
DepthAnything	100%	1.91	1.79	1.51	0.62	0.00	0.00	0.00	0.00
MVSFormer (0)	100%	1.08	0.47	0.41	0.50	0.68	0.16	0.40	0.52
MVSFormer++ (0)	100%	0.67	0.28	0.24	0.33	0.79	0.22	0.53	0.65
GeoMVSNet (0)	100%	1.19	0.61	0.77	0.36	0.53	0.05	0.18	0.28
MVSFormer (0.25)	90%	1.09	0.46	0.38	0.38	0.72	0.16	0.40	0.51
MVSFormer++ (0.25)	88%	0.61	0.22	0.19	0.14	0.86	0.22	0.52	0.63
GeoMVSNet (0.25)	100%	1.19	0.61	0.77	0.36	0.53	0.05	0.18	0.28
MVSFormer (0.5)	47%	0.52	0.16	0.10	0.06	0.93	0.14	0.30	0.36
MVSFormer++ (0.5)	62%	0.26	0.10	0.07	0.04	0.96	0.19	0.43	0.50
GeoMVSNet (0.5)	23%	1.45	0.90	1.11	0.48	0.38	0.00	0.02	0.04
Ours	100%	0.16	0.09	0.07	0.10	0.93	0.21	0.58	0.76

Table 2. Results on the Scannet++ dataset [67]. Numbers in brackets indicate the confidence thresholding for MVSNet methods.

As an established representative of patch match-based methods, we also compared with photometric depth maps generated by COLMAP [41]. Finally, we compared with the recent indoor-specialized metric configuration of the monocular depth estimator DepthAnything [63]. Our results were produced using hyperparameters as described in 5.2 and the supplemental. For initial depth estimations we use Marigold [21].

We consider the standard error metrics root mean squared error (RMSE), mean absolute error (MAE), L1-rel [50], L1-inv [50], δ_1 [63]. We also calculate the accuracy of estimated depth samples ($|z - z_{GT}| < \tau$) considering different thresholds τ . Results with values in the upper 20 percent are marked in green, the greener the better.

Overall, our approach performed best for the synthetic Replica dataset, as shown in Tab. 1, independently of the quality of the point cloud. Ours+ refers to good point clouds (2% noise + 2% outliers), Ours- to poor point clouds (5-10% noise + 5-10% outliers, see supplemental material for further details). While surprisingly robust, differences to ground truth are notable especially with very poor point cloud input.

Quantitative results for Scannet++ are shown in Tab. 2. Regarding completeness (valid samples), RMSE, MAS, L1-rel, and Accuracy $\tau=0.05$ and $\tau=0.1$, we performed best or on par overall. Only for L1-inv, δ_1 , and accuracy with $\tau = 0.01$, MVSFormer++ with certainty threshold of 0.5 performed slightly better. However, for this configuration only 62% of the values were actually considered for the mean metric, while our results were evaluated on nearly all available samples ($> 99.5\%$).

Qualitative results of both the Replica and the Scan-

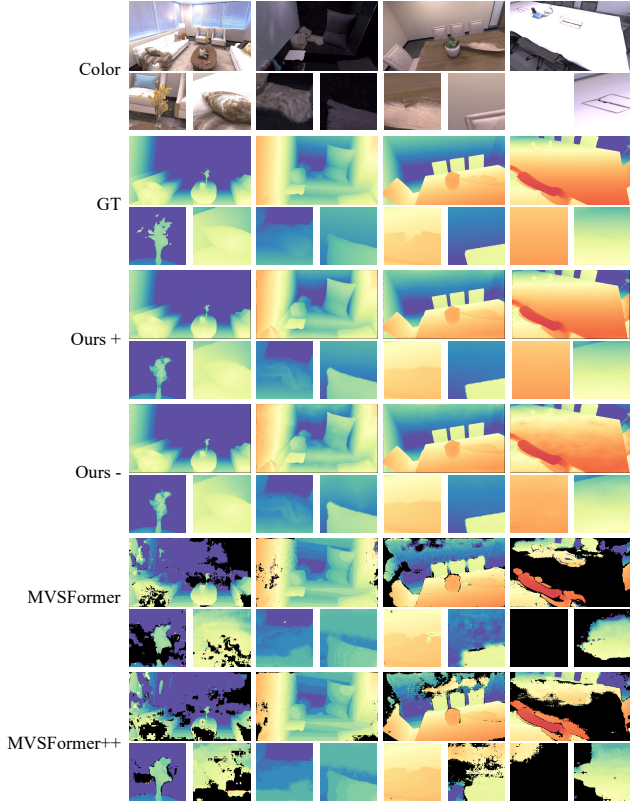


Figure 5. Qualitative results on the Replica dataset. Certainty threshold of MVSFormers was set to the their default of 0.5.

Net++ dataset are shown in Figs. 5 and 6. Our results are clean, dense and plausible. However, artifact are notable at the glossy table in Scene 3. Sometimes our solutions are even more complete than the ground truth, for examples see ventilator and lamp (Scene 4, left and right crop) or, the leg of the table (Scene5, right crop). Results of MVSNet-likes are sparse and especially walls appear noisy. The metric version of DepthAnything shows very promising geometric details, however, the global scale is inaccurate.

5.2. Ablation Studies

In this section, we finetune hyper parameters and present ablation studies based on seven scenes of the Scannet++ dataset. Further ablation studies are in the Appendix C.

Losses. As presented in Tab. 3, using only \mathcal{L}_{geo} yields sub-optimal results. Combining \mathcal{L}_{geo} with \mathcal{L}_{photo} without regularizers performs poorly, indicating that integrating photometric consistency as objective term is non-trivial and can become unstable. The combination of \mathcal{L}_{geo} with \mathcal{R}_p significantly outperforms a simple \mathcal{R}_s , demonstrating the importance of more sophisticated regularization. Adding the second mono depth map-based regularizer \mathcal{R}_e , which aims to preserve or recover edges, further improves the results.

Setup	RMSE	MAE	L1-rel	L1-inv	Acc. 0.01 m	Acc. 0.05 m	Acc. 0.10 m
\mathcal{L}_{geo}	0.32	0.13	0.15	0.15	0.14	0.45	0.65
$\mathcal{L}_{geo} + \mathcal{L}_{photo}$	0.86	0.37	0.42	0.27	0.17	0.39	0.51
$\mathcal{L}_{geo} + \mathcal{R}_s$	0.26	0.12	0.12	0.15	0.14	0.45	0.65
$\mathcal{L}_{geo} + \mathcal{R}_p$	0.22	0.11	0.12	0.12	0.16	0.53	0.74
$\mathcal{L}_{geo} + \mathcal{R}_p + \mathcal{R}_e$	0.21	0.10	0.11	0.10	0.16	0.55	0.76
$\mathcal{L}_{geo} + \mathcal{R}_s + \mathcal{R}_p + \mathcal{R}_e$	0.21	0.10	0.11	0.10	0.16	0.55	0.76
$\mathcal{L}_{geo} + \mathcal{L}_{photo} + \mathcal{R}_p + \mathcal{R}_e$	0.22	0.10	0.12	0.13	0.22	0.57	0.75
$\mathcal{L}_{geo} + \mathcal{L}_{photo} + \mathcal{R}_s + \mathcal{R}_p + \mathcal{R}_e$	0.22	0.10	0.11	0.12	0.22	0.57	0.75
$\mathcal{L}_{geo} + \mathcal{L}_{photo,local} + \mathcal{R}_p + \mathcal{R}_e$	0.21	0.10	0.11	0.10	0.23	0.59	0.77
$\mathcal{L}_{geo} + \mathcal{L}_{photo,local} + \mathcal{R}_s + \mathcal{R}_p + \mathcal{R}_e$	0.21	0.10	0.11	0.10	0.23	0.60	0.77

Table 3. Ablation study for our training losses.

Setup	RMSE	MAE	L1-rel	L1-inv	δ_{\perp}	Acc. 0.01 m	Acc. 0.05 m	Acc. 0.10 m
Coarse: none + Local: default	0.23	0.14	0.15	0.25	0.82	0.14	0.39	0.58
Coarse: (o^g, s^g) + Local: default	0.16	0.08	0.08	0.13	0.91	0.24	0.61	0.77
Coarse: MLP _S + Local: default	0.18	0.09	0.09	0.11	0.92	0.25	0.63	0.80
Coarse: MLP _M + Local: default	0.20	0.09	0.10	0.14	0.92	0.25	0.64	0.80
Coarse: MLP _{XL} + Local: none	0.42	0.32	0.40	0.31	0.65	0.05	0.22	0.37

Table 4. Ablation study for coarse and local refinement.

Incorporating photometric consistency with regularizers notably boosts accuracy metrics, suggesting that local refinement with color loss is highly effective, though it does not improve coarse alignment. This is confirmed by the ablation studies where the photometric loss was applied only during local ($\mathcal{L}_{photo,local}$), but not coarse, refinement. Based on these findings, we chose to use all regularizers and use the \mathcal{L}_{photo} only during local refinement.

Coarse & Local Refinement As presented in Tab. 4, only using a very large MLP_{XL} (four hidden layers, width 128, $m=6$ and $k=16$, m and k as introduced in Section 3.6) optimized using proposed losses without local refinement performed subpar. Same holds for skipping the coarse alignment.

Using an MLP_M (two hidden layers, width 32, $m=3$ and $k=5$), MLP_S (two hidden layers, width 16, $m=3$ and $k=5$), or only global (o^g, s^g) as optimized parameters during the coarse refinement produced similar results. Using only (o^g, s^g) results in low errors in terms of distance-based metrics but poor accuracy (see e.g. $\tau = 0.1$), highlighting a lack of precision in the overall alignment. The MLP_M produced higher distance errors but better accuracy, indicating potential overfitting to sparse points but overshooting in regions with scarce data. The MLP_S states a middle ground, effectively combining the strengths of both by offering a balanced trade-off between accuracy and robustness.

6. Limitations

While our approach demonstrates robust performance, several limitations remain.

Photometric consistency, though generally effective, can become a pitfall in scenarios involving specular materials, changing lighting conditions, or variations in white balance, leading to degraded results that our method will not mitigate.

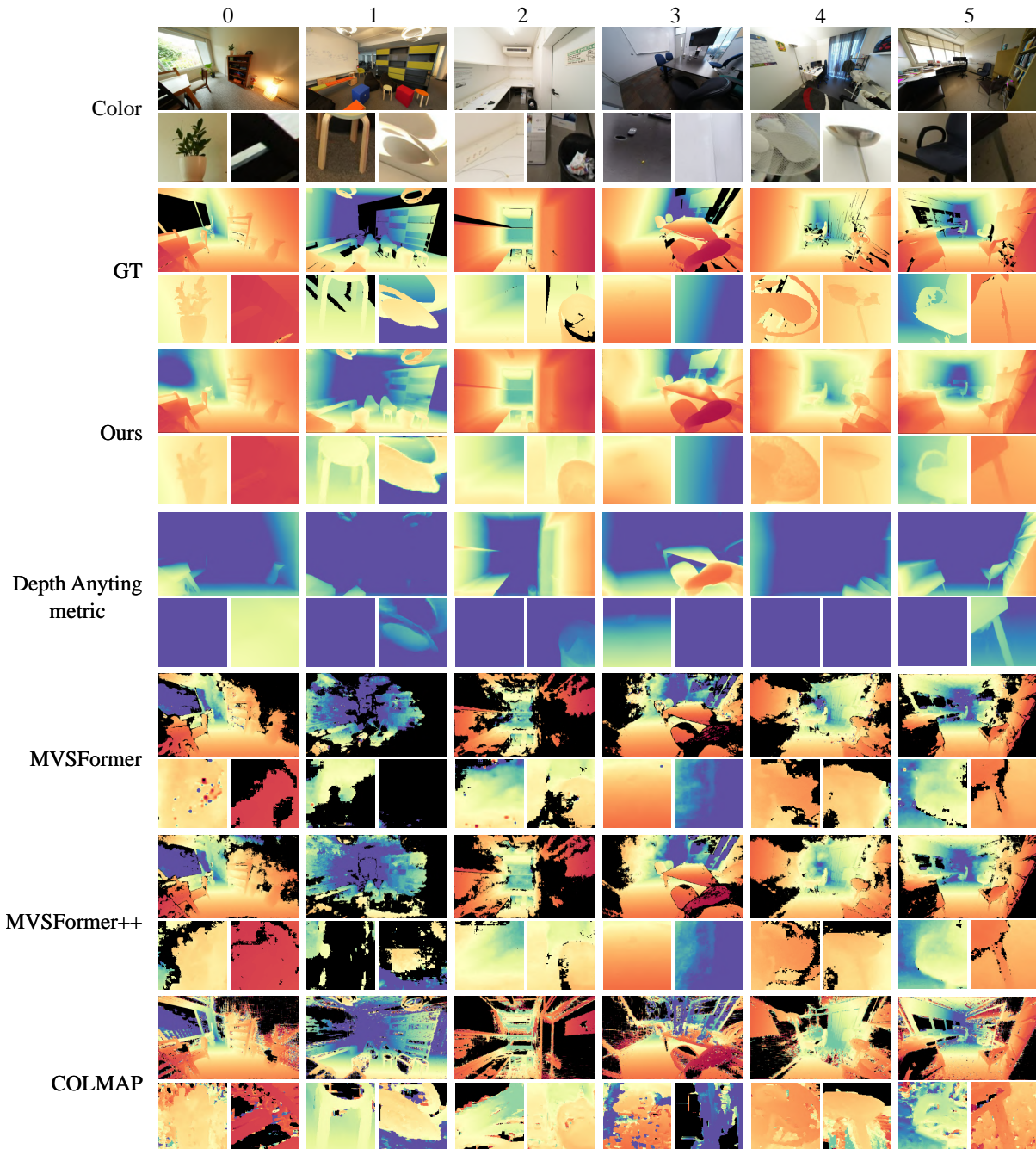


Figure 6. Qualitative results on the ScanNet++ dataset. Certainty threshold of MVSFormers was set to the their default of 0.5.

As shown in Sec. 5.1, outliers in the sparse point cloud can result in spurious outcomes, affecting the overall accuracy and reliability of the depth estimation.

Finally, our method is dependent on the quality of the initial monocular depth map to establish a valid scene topology prior. This especially pertains to the availability of a good edge image to accurately mask out occluded regions which our losses rely on. Any deficiencies in these starting points

can propagate through the subsequent steps, impacting the final results.

7. Conclusion

In conclusion, our approach demonstrates that monocular depth maps can be significantly improved by incorporating photometric consistency, leading to enhanced depth estimation. By utilizing a meshed version of the monocular depth

map, we directly leverage the strong initial estimates and achieve stable optimization when handled correctly. In this context, our Poisson and edge regularizers have proven to be particularly effective, ensuring robust and reliable depth map refinement. Our simple yet effective pipeline consistently produces accurate and very dense depth maps, which is highly desirable for many downstream tasks.

8. Acknowledgments

We would like to thank all members of the Visual Computing Lab Erlangen for the fruitful discussions. Specifically, we appreciate Darius Rückert’s support during late night debugging sessions. The authors gratefully acknowledge the scientific support and HPC resources provided by the National High Performance Computing Center of the Friedrich-Alexander-Universität Erlangen-Nürnberg (NHR@FAU) under the project b212dc. NHR funding is provided by federal and Bavarian state authorities. NHR@FAU hardware is partially funded by the German Research Foundation (DFG) – 440719683. Linus Franke was supported by the 5G innovation program of the German Federal Ministry for Digital and Transport under the funding code 165GU103B. Joachim Keinert was supported by the Free State of Bavaria in the DSAI project.

References

- [1] Michael Bleyer, Christoph Rhemann, and Carsten Rother. Patchmatch stereo-stereo matching with slanted support windows. In *Bmvc*, pages 1–11, 2011. [1](#), [2](#)
- [2] Samuel R Buss. *3D computer graphics: a mathematical introduction with OpenGL*. Cambridge University Press, 2003. [6](#), [14](#)
- [3] Chenjie Cao, Xinlin Ren, and Yanwei Fu. MVFormer: Multi-view stereo by learning robust image features and temperature-based depth. *Trans. Mach. Learn. Res.*, 2022, 2022. [2](#), [7](#)
- [4] Shuo Cheng, Zexiang Xu, Shilin Zhu, Zhuwen Li, Li Erran Li, Ravi Ramamoorthi, and Hao Su. Deep stereo using adaptive thin volume representation with uncertainty awareness. In *Proceedings of the IEEE/CVF Conference on Computer Vision and Pattern Recognition*, pages 2524–2534, 2020. [2](#)
- [5] Xinlin Ren Chenjie Cao and Yanwei Fu. MVFormer++: Revealing the devil in transformer’s details for multi-view stereo. In *International Conference on Learning Representations (ICLR)*, 2024. [2](#), [7](#)
- [6] Ilya Chugunov, Yuxuan Zhang, and Felix Heide. Shakes on a plane: Unsupervised depth estimation from unstabilized photography. In *Proceedings of the IEEE/CVF Conference on Computer Vision and Pattern Recognition*, pages 13240–13251, 2023. [3](#)
- [7] Papers With Code. Point Clouds on Tanks and Temples Benchmark. [2](#)
- [8] Robert T Collins. A space-sweep approach to true multi-image matching. In *Proceedings CVPR IEEE Computer Society Conference on Computer Vision and Pattern Recognition*, pages 358–363. Ieee, 1996. [2](#)
- [9] Yikang Ding, Wentao Yuan, Qingtian Zhu, Haotian Zhang, Xiangyue Liu, Yuanjiang Wang, and Xiao Liu. Transmvsnet: Global context-aware multi-view stereo network with transformers. In *Proceedings of the IEEE/CVF Conference on Computer Vision and Pattern Recognition*, pages 8585–8594, 2022. [2](#)
- [10] Laura Fink, Darius Rückert, Linus Franke, Joachim Keinert, and Marc Stamminger. Livenvs: Neural view synthesis on live rgb-d streams. In *SIGGRAPH Asia 2023 Conference Papers*, pages 1–11, 2023. [2](#)
- [11] Michael Garland and Paul S Heckbert. Surface simplification using quadric error metrics. In *Proceedings of the 24th Annual Conference on Computer Graphics and Interactive Techniques*, pages 209–216, 1997. [4](#)
- [12] Yongtao Ge, Guangkai Xu, Zhiyue Zhao, Libo Sun, Zheng Huang, Yanlong Sun, Hao Chen, and Chunhua Shen. GeoBench: Benchmarking and analyzing monocular geometry estimation models. *arXiv preprint arXiv:2406.12671*, 2024. [1](#), [3](#)
- [13] Tobias Gruber, Frank Julca-Aguilar, Mario Bijelic, and Felix Heide. Gated2depth: Real-time dense lidar from gated images. In *Proceedings of the IEEE/CVF International Conference on Computer Vision*, pages 1506–1516, 2019. [1](#), [3](#)
- [14] Xiaodong Gu, Zhiwen Fan, Siyu Zhu, Zuozhuo Dai, Feitong Tan, and Ping Tan. Cascade cost volume for high-resolution multi-view stereo and stereo matching. In *Proceedings of the IEEE/CVF conference on computer vision and pattern recognition*, pages 2495–2504, 2020. [2](#)
- [15] Bjoern Haefner, Yvain Quéau, Thomas Möllenhoff, and Daniel Cremers. Fight ill-posedness with ill-posedness: Single-shot variational depth super-resolution from shading. In *Proceedings of the IEEE Conference on Computer Vision and Pattern Recognition*, pages 164–174, 2018. [3](#)
- [16] Richard Hartley and Andrew Zisserman. *Multiple View Geometry in Computer Vision*. Cambridge university press, 2003. [1](#), [2](#)
- [17] Peter Hedman, Julien Philip, True Price, Jan-Michael Frahm, George Drettakis, and Gabriel Brostow. Deep blending for free-viewpoint image-based rendering. *ACM Transactions on Graphics (ToG)*, 37(6):1–15, 2018. [2](#)
- [18] Peter J Huber. Robust estimation of a location parameter. In *Breakthroughs in Statistics: Methodology and Distribution*, pages 492–518. Springer, 1992. [6](#)
- [19] Shintaro Ito, Kanta Miura, Koichi Ito, and Takafumi Aoki. Neural radiance field-inspired depth map refinement for accurate multi-view stereo. *Journal of Imaging*, 10(3):68, 2024. [3](#)
- [20] Achuta Kadambi, Vage Taamazyan, Boxin Shi, and Ramesh Raskar. Depth sensing using geometrically constrained polarization normals. *International Journal of Computer Vision*, 125:34–51, 2017. [3](#)
- [21] Bingxin Ke, Anton Obukhov, Shengyu Huang, Nando Metzger, Rodrigo Caye Daudt, and Konrad Schindler. Repurposing diffusion-based image generators for monocular depth estimation. In *Proceedings of the IEEE/CVF Conference*

- on *Computer Vision and Pattern Recognition*, pages 9492–9502, 2024. 1, 2, 3, 4, 7, 14
- [22] Leonid Keselman, John Iselin Woodfill, Anders Grunnet-Jepsen, and Achintya Bhowmik. Intel realsense stereoscopic depth cameras. In *Proceedings of the IEEE Conference on Computer Vision and Pattern Recognition Workshops*, pages 1–10, 2017. 2
- [23] Subin Kim, Seong Hyeon Park, Sihyun Yu, Kihyuk Sohn, and Jinwoo Shin. MC2: Multi-view consistent depth estimation via coordinated image-based neural rendering. 3
- [24] DP Kingma. Adam: A method for stochastic optimization. *arXiv preprint arXiv:1412.6980*, 2014. 14
- [25] Arno Knapitsch, Jaesik Park, Qian-Yi Zhou, and Vladlen Koltun. Tanks and Temples: Benchmarking Large-Scale Scene Reconstruction. *ACM Transactions on Graphics*, 36(4), 2017. 2, 7
- [26] Samuli Laine, Janne Hellsten, Tero Karras, Yeongho Seol, Jaakko Lehtinen, and Timo Aila. Modular primitives for high-performance differentiable rendering. *ACM Transactions on Graphics*, 39(6), 2020. 2, 6, 14
- [27] Jiahe Li, Jiawei Zhang, Xiao Bai, Jin Zheng, Xin Ning, Jun Zhou, and Lin Gu. Dngaussian: Optimizing sparse-view 3d gaussian radiance fields with global-local depth normalization. In *Proceedings of the IEEE/CVF Conference on Computer Vision and Pattern Recognition*, pages 20775–20785, 2024. 3
- [28] You Li and Javier Ibanez-Guzman. Lidar for autonomous driving: The principles, challenges, and trends for automotive lidar and perception systems. *IEEE Signal Processing Magazine*, 37(4):50–61, 2020. 1, 2
- [29] Zhengqi Li, Qianqian Wang, Forrester Cole, Richard Tucker, and Noah Snavely. Dynibar: Neural dynamic image-based rendering. In *Proceedings of the IEEE/CVF Conference on Computer Vision and Pattern Recognition*, pages 4273–4284, 2023. 3
- [30] Jinli Liao, Yikang Ding, Yoli Shavit, Dihe Huang, Shihao Ren, Jia Guo, Wensen Feng, and Kai Zhang. Wt-mvsnet: window-based transformers for multi-view stereo. *Advances in Neural Information Processing Systems*, 35:8564–8576, 2022. 2
- [31] Tianqi Liu, Xinyi Ye, Weiyue Zhao, Zhiyu Pan, Min Shi, and Zhiguo Cao. When epipolar constraint meets non-local operators in multi-view stereo. In *Proceedings of the IEEE/CVF International Conference on Computer Vision*, pages 18088–18097, 2023. 2
- [32] Fangchang Ma, Guilherme Venturelli Cavalheiro, and Sertac Karaman. Self-supervised sparse-to-dense: Self-supervised depth completion from lidar and monocular camera. In *2019 International Conference on Robotics and Automation (ICRA)*, pages 3288–3295. IEEE, 2019. 1, 3
- [33] Parsa Mirdehghan, Maxx Wu, Wenzheng Chen, David B Lindell, and Kiriakos N Kutulakos. TurboSL: Dense Accurate and Fast 3D by Neural Inverse Structured Light. 3
- [34] Thomas Müller, Alex Evans, Christoph Schied, and Alexander Keller. Instant neural graphics primitives with a multiresolution hash encoding. *ACM transactions on graphics (TOG)*, 41(4):1–15, 2022. 3
- [35] Roy Or-El, Guy Rosman, Aaron Wetzler, Ron Kimmel, and Alfred M Bruckstein. Rgb-d-fusion: Real-time high precision depth recovery. In *Proceedings of the IEEE Conference on Computer Vision and Pattern Recognition*, pages 5407–5416, 2015. 3
- [36] Roy Or-El, Rom Hershkovitz, Aaron Wetzler, Guy Rosman, Alfred M Bruckstein, and Ron Kimmel. Real-time depth refinement for specular objects. In *Proceedings of the IEEE Conference on Computer Vision and Pattern Recognition*, pages 4378–4386, 2016. 3
- [37] Patrick Pérez, Michel Gangnet, and Andrew Blake. Poisson image editing. In *ACM SIGGRAPH 2003 Papers*, pages 313–318. 2003. 2, 6
- [38] Antoni Rosinol, John J Leonard, and Luca Carlone. Nerfslam: Real-time dense monocular slam with neural radiance fields. In *2023 IEEE/RSJ International Conference on Intelligent Robots and Systems (IROS)*, pages 3437–3444. IEEE, 2023. 7
- [39] Daniel Scharstein and Richard Szeliski. High-accuracy stereo depth maps using structured light. In *2003 IEEE Computer Society Conference on Computer Vision and Pattern Recognition, 2003. Proceedings.*, pages I–I. IEEE, 2003. 2
- [40] Johannes L Schonberger and Jan-Michael Frahm. Structure-from-motion revisited. In *Proceedings of the IEEE Conference on Computer Vision and Pattern Recognition*, pages 4104–4113, 2016. 4, 7, 14
- [41] Johannes Lutz Schönberger, Enliang Zheng, Marc Pollefeys, and Jan-Michael Frahm. Pixelwise view selection for unstructured multi-view stereo. In *European Conference on Computer Vision (ECCV)*, 2016. 2, 7, 14
- [42] Aarushi Shandilya, Benjamin Attal, Christian Richardt, James Tompkin, and Matthew O’toole. Neural fields for structured lighting. In *Proceedings of the IEEE/CVF International Conference on Computer Vision*, pages 3512–3522, 2023. 3
- [43] Documentation Stereolabs. Depth sensing: Depth settings, 2023. 1, 2
- [44] Vladimiro Sterzentsenko, Leonidas Saroglou, Anargyros Chatzitofis, Spyridon Thermos, Nikolaos Zioulis, Alexandros Domanoglou, Dimitrios Zarpalas, and Petros Daras. Self-supervised deep depth denoising. In *Proceedings of the IEEE/CVF International Conference on Computer Vision*, pages 1242–1251, 2019. 3
- [45] Eli Stevens, Luca Antiga, and Thomas Viehmann. *Deep Learning with PyTorch*. Manning Publications, 2020. 14
- [46] Julian Straub, Thomas Whelan, Lingni Ma, Yufan Chen, Erik Wijmans, Simon Green, Jakob J Engel, Raul Mur-Artal, Carl Ren, Shobhit Verma, et al. The Replica dataset: A digital replica of indoor spaces. *arXiv preprint arXiv:1906.05797*, 2019. 7
- [47] Zhanghao Sun, Wei Ye, Jinhui Xiong, Gyeongmin Choe, Jialiang Wang, Shuochen Su, and Rakesh Ranjan. Consistent direct time-of-flight video depth super-resolution. In *Proceedings of the IEEE/CVF Conference on Computer Vision and Pattern Recognition*, pages 5075–5085, 2023. 3
- [48] Matthew Tancik, Pratul P. Srinivasan, Ben Mildenhall, Sara Fridovich-Keil, Nithin Raghavan, Utkarsh Singhal, Ravi Ra-

- mamoorthi, Jonathan T. Barron, and Ren Ng. Fourier features let networks learn high frequency functions in low dimensional domains. *NeurIPS*, 2020. 5
- [49] Michael W Tao, Pratul P Srinivasan, Jitendra Malik, Szymon Rusinkiewicz, and Ravi Ramamoorthi. Depth from shading, defocus, and correspondence using light-field angular coherence. In *Proceedings of the IEEE Conference on Computer Vision and Pattern Recognition*, pages 1940–1948, 2015. 3
- [50] Benjamin Ummenhofer, Huizhong Zhou, Jonas Uhrig, Nikolaus Mayer, Eddy Ilg, Alexey Dosovitskiy, and Thomas Brox. Demon: Depth and motion network for learning monocular stereo. In *Proceedings of the IEEE Conference on Computer Vision and Pattern Recognition*, pages 5038–5047, 2017. 7
- [51] Ulla Wandinger. Introduction to lidar. In *Lidar: Range-Resolved Optical Remote Sensing of the Atmosphere*, pages 1–18. Springer, 2005. 2
- [52] Qianqian Wang, Zhicheng Wang, Kyle Genova, Pratul P Srinivasan, Howard Zhou, Jonathan T Barron, Ricardo Martin-Brualla, Noah Snavely, and Thomas Funkhouser. Ibrnet: Learning multi-view image-based rendering. In *Proceedings of the IEEE/CVF Conference on Computer Vision and Pattern Recognition*, pages 4690–4699, 2021. 2, 3
- [53] Xiang Wang, Chen Wang, Bing Liu, Xiaoqing Zhou, Liang Zhang, Jin Zheng, and Xiao Bai. Multi-view stereo in the Deep Learning Era: A comprehensive review. *Displays*, 70: 102102, 2021. 1
- [54] Yuesong Wang, Zhaojie Zeng, Tao Guan, Wei Yang, Zhuo Chen, Wenkai Liu, Luoyuan Xu, and Yawei Luo. Adaptive patch deformation for textureless-resilient multi-view stereo. In *Proceedings of the IEEE/CVF Conference on Computer Vision and Pattern Recognition*, pages 1621–1630, 2023. 2
- [55] Zizhuang Wei, Qingtian Zhu, Chen Min, Yisong Chen, and Guoping Wang. Aa-rmvnsnet: Adaptive aggregation recurrent multi-view stereo network. In *Proceedings of the IEEE/CVF International Conference on Computer Vision (ICCV)*, pages 6187–6196, 2021. 2
- [56] Suttisak Wizadwongsa, Pakkapon Phongthawee, Jiraphon Yenphraphai, and Supasorn Suwajanakorn. Nex: Real-time view synthesis with neural basis expansion. In *Proceedings of the IEEE/CVF Conference on Computer Vision and Pattern Recognition*, pages 8534–8543, 2021. 2, 3
- [57] Chenglei Wu, Michael Zollhöfer, Matthias Nießner, Marc Stamminger, Shihram Izadi, and Christian Theobalt. Real-time shading-based refinement for consumer depth cameras. *ACM Transactions on Graphics (ToG)*, 33(6):1–10, 2014. 3
- [58] Qingshan Xu and Wenbing Tao. Multi-scale geometric consistency guided multi-view stereo. In *Proceedings of the IEEE/CVF Conference on Computer Vision and Pattern Recognition*, pages 5483–5492, 2019. 2
- [59] Qingshan Xu, Weihang Kong, Wenbing Tao, and Marc Pollefeys. Multi-scale geometric consistency guided and planar prior assisted multi-view stereo. *IEEE Transactions on Pattern Analysis and Machine Intelligence*, 45(4):4945–4963, 2022. 2, 4
- [60] Jianfeng Yan, Zizhuang Wei, Hongwei Yi, Mingyu Ding, Runze Zhang, Yisong Chen, Guoping Wang, and Yu-Wing Tai. Dense hybrid recurrent multi-view stereo net with dynamic consistency checking. In *Computer Vision—ECCV 2020: 16th European Conference, Glasgow, UK, August 23–28, 2020, Proceedings, Part IV*, pages 674–689. Springer, 2020. 2
- [61] Shi Yan, Chenglei Wu, Lizhen Wang, Feng Xu, Liang An, Kaiwen Guo, and Yebin Liu. Ddrnet: Depth map denoising and refinement for consumer depth cameras using cascaded cnns. In *Proceedings of the European Conference on Computer Vision (ECCV)*, pages 151–167, 2018. 3
- [62] Jiayu Yang, Wei Mao, Jose M Alvarez, and Miaomiao Liu. Cost volume pyramid based depth inference for multi-view stereo. In *Proceedings of the IEEE/CVF Conference on Computer Vision and Pattern Recognition*, pages 4877–4886, 2020. 2
- [63] Lihe Yang, Bingyi Kang, Zilong Huang, Xiaogang Xu, Jiashi Feng, and Hengshuang Zhao. Depth anything: Unleashing the power of large-scale unlabeled data. In *Proceedings of the IEEE/CVF Conference on Computer Vision and Pattern Recognition*, pages 10371–10381, 2024. 1, 3, 7
- [64] Lihe Yang, Bingyi Kang, Zilong Huang, Zhen Zhao, Xiaogang Xu, Jiashi Feng, and Hengshuang Zhao. Depth anything V2. *arXiv preprint arXiv:2406.09414*, 2024. 1, 3
- [65] Yao Yao, Zixin Luo, Shiwei Li, Tian Fang, and Long Quan. Mvsnet: Depth inference for unstructured multi-view stereo. In *Proceedings of the European Conference on Computer Vision (ECCV)*, pages 767–783, 2018. 1, 2, 7
- [66] Yao Yao, Zixin Luo, Shiwei Li, Tianwei Shen, Tian Fang, and Long Quan. Recurrent mvsnet for high-resolution multi-view stereo depth inference. In *Proceedings of the IEEE/CVF conference on computer vision and pattern recognition*, pages 5525–5534, 2019. 2
- [67] Chandan Yeshwanth, Yueh-Cheng Liu, Matthias Nießner, and Angela Dai. Scannet++: A high-fidelity dataset of 3d indoor scenes. In *Proceedings of the IEEE/CVF International Conference on Computer Vision*, pages 12–22, 2023. 7, 14
- [68] Ming-Ze Yuan, Lin Gao, Hongbo Fu, and Shihong Xia. Temporal upsampling of depth maps using a hybrid camera. *IEEE transactions on visualization and computer graphics*, 25(3):1591–1602, 2018. 3
- [69] Zhenlong Yuan, Jiakai Cao, Zhaoyi Wang, and Zhaoxin Li. Tsar-mvs: Textureless-aware segmentation and correlative refinement guided multi-view stereo. *Pattern Recognition*, 154:110565, 2024. 2
- [70] Aviad Zabatani, Vitaly Surazhsky, Erez Sperling, Sagi Ben Moshe, Ohad Menashe, David H Silver, Zach Karni, Alexander M Bronstein, Michael M Bronstein, and Ron Kimmel. Intel® realsense™ sr300 coded light depth camera. *IEEE transactions on pattern analysis and machine intelligence*, 42(10):2333–2345, 2019. 1, 2
- [71] Pietro Zanuttigh, Giulio Marin, Carlo Dal Mutto, Fabio Dominio, Ludovico Minto, Guido Maria Cortelazzo, et al. Time-of-flight and structured light depth cameras. *Technology and Applications*, 978(3), 2016. 1, 2
- [72] Junming Zhang, Manikandasriram Srinivasan Ramanagopal, Ram Vasudevan, and Matthew Johnson-Roberson. Listereo: Generate dense depth maps from lidar and stereo imagery.

In *2020 IEEE International Conference on Robotics and Automation (ICRA)*, pages 7829–7836. IEEE, 2020. 3

- [73] Mingfang Zhang, Jinglu Wang, Xiao Li, Yifei Huang, Yoichi Sato, and Yan Lu. Structural multiplane image: Bridging neural view synthesis and 3d reconstruction. In *Proceedings of the IEEE/CVF Conference on Computer Vision and Pattern Recognition*, pages 16707–16716, 2023. 2
- [74] Zhe Zhang, Rui Peng, Yuxi Hu, and Ronggang Wang. Geomvsnet: Learning multi-view stereo with geometry perception. In *Proceedings of the IEEE/CVF Conference on Computer Vision and Pattern Recognition*, pages 21508–21518, 2023. 7
- [75] Qingtian Zhu, Chen Min, Zizhuang Wei, Yisong Chen, and Guoping Wang. Deep learning for multi-view stereo via plane sweep: A survey. *arXiv preprint arXiv:2106.15328*, 2021. 1, 2

A. Implementation and Training Details

For our implementation, we use the hardware accelerated framework NVDiffRast [26] with the adjusted formulation outlined in Main-Sec. 4. For initial depth estimations we use Marigold [21] and employ COLMAP [40, 41] for Structure-from-Motion and image undistortion with configurations as recommended by the used dataset [67]. In Fig. 7, we depict sparse pointclouds of representative views, showcasing sparseness especially on white walls. For coarse refinement, Ψ is a shallow MLP with degrees of positional encoding being $m = 3$ and $k = 5$. Two hidden layers of width 16, initialized with a normal distribution with $\sigma = 0.1$. This comparatively small initialization ensures o_g and s_g start of very small, stabilizing training. During the coarse refinement phase, we used a learning rate of 0.001 and stop after 400 iterations with batch sizes of 22. The current states of o_g and s_g are baked into M’s z . We stop optimization after another 700 iterations of local refinement with learning rates of 0.0005. In total, the process takes around 12 min per depth map but we see huge potential for performance improvements. The used losses were weighted as documented in Tab. 5. We used the Adam [24] optimizer with default parameters as proposed by the PyTorch framework [45].

Loss		Regularizer	
\mathcal{L}_{photo}	1.0	\mathcal{R}_p	400.0
\mathcal{L}_{geo}	0.1	\mathcal{R}_e	0.1
		\mathcal{R}_s	0.001

Table 5. Used weights for computing the total optimization loss.

Projection Matrices. We convert the intrinsics definition C with $\{f_x, f_y, c_x, c_y\}$ to the projection matrix P following the OpenGL convention [2], with $d_{near} = 0.1$ and $d_{far} = 100$ using

$$P = \begin{pmatrix} \frac{2f_x}{W} & 0 & 1 - \frac{2c_x}{W} & 0 \\ 0 & -\frac{2f_y}{H} & 1 - \frac{2c_y}{H} & 0 \\ 0 & 0 & -\frac{(d_{far} + d_{near})}{d_{near} - d_{far}} & -\frac{2d_{far}d_{near}}{d_{far} - d_{near}} \\ 0 & 0 & -1 & 0 \end{pmatrix}. \quad (19)$$

B. Datasets

For the ScanNet++ dataset, ground truth depth maps are rendered from the meshes, for the sparse point cloud, poses, and undistortion, we employed COLMAP [40] as proposed by the dataset toolkit [67].

For the results present in Main-Sec. 5.1, we used 10 scenes from the ScanNet++ validation set and 10 depth maps of each (100 in total). These scenes have consecutive frames and less than 15% of the views being marked as blurry. To tune the hyperparameters of our approach (see Main-Sec. 5.2), such as MLP configuration or decimation,

Setup	RMSE	MAE	L1-rel	L1-inv	Acc. 0.01 m	Acc. 0.05 m	Acc. 0.10 m
$d = 4, r = 1$	0.203	0.088	0.091	0.078	0.26	0.65	0.82
$d = 4, r = 0.5$	0.198	0.087	0.090	0.080	0.25	0.64	0.81
$d = 4, r = 0.25$	0.202	0.090	0.095	0.084	0.25	0.63	0.80
$d = 8, r = 1$	0.213	0.098	0.106	0.095	0.23	0.60	0.77
$d = 8, r = 0.5$	0.214	0.100	0.109	0.099	0.23	0.59	0.77
$d = 8, r = 0.25$	0.216	0.101	0.110	0.101	0.22	0.58	0.76

Table 6. Ablation study on downsampling factor d and decimation ratio r . A higher value of d indicates lower geometric resolution, while a higher value of r indicates a higher geometric resolution.

we prepared another, different seven scenes with 10 views each (70 in total) in an analogous manner. Note that these seven scenes have not been used in the further evaluation. The hyperparameters found in the ablation studies were used consistently for all results showcased in the Main-Sec. 5.1.

For the Replica dataset, color and ground truth depth maps are obtained from the rendered meshes. We selected four scenes, and optimized 64 depth maps for each. As sparse point clouds, we generated 5000 point samples from the ground truth depth map, added a relative error with standard deviation of 2%, and randomly replaced 2% by randomly distributed outliers from the overall depth range. To examine the impact of the quality of the point cloud, we also generated worse point clouds: for two scenes (room0 and room2) we went down to 3500 points with relative error of 5% and 5% outliers, and for scenes officel and office4 only 1000 points were generated, with a relative error of 10% and 10% outliers. The numbers were chosen to match approximately match the error distribution as observed in real-world scenarios, see Fig. 7. Nevertheless, the uniform density of the constructed sparse point clouds is unrealistic which may limit expressiveness.

To optimize for photo-consistency, we used 60 auxiliary views for the Replica dataset and 30 for Scannet++. MVSFormer, MVSFormer++ and GeoMVSNet received their default amount of 10 views as input which were evenly distributed across the set of our auxiliary views.

C. Further Ablation studies

Mesh Decimation. Setting the initial downsample factor to $d = 4$ (reducing 1738k values in the depth map to 224k vertices) showed consistently better results than $d = 8$, as shown in Tab. 6.

Mesh decimation ratios r of 1.0, 0.5 (reducing to 112k vertices), and 0.25 (56k vertices) show very negligible differences, with 0.5 slightly outperforming 1.0 on some metrics. Based on this, we chose $r = 0.5$ as the default.

Initial Depth Estimation. Comparing different monocular depth estimation techniques (see Tab. 7), both Marigold and Depth Anything Large (L) perform nearly equally well. This suggests our method might benefit from future ad-



Figure 7. Visualization of the *visible* sparse pointclouds from SfM of different representative views. Color of the points encodes the relative depth error compared to the groundtruth depth map. Number of points and standard deviation of the relative error was, from left to right: 1.7k and 9.2 %, 3.3k and 5.7 %, and 6k and 3.5 %.

Setup	RMSE	MAE	L1-rel	L1-inv	δ_1	Acc. 0.01 m	Acc. 0.05 m	Acc. 0.10 m
Marigold	0.18	0.09	0.09	0.10	0.92	0.25	0.63	0.79
DepthAnythingS	0.21	0.10	0.11	0.13	0.91	0.21	0.56	0.75
DepthAnythingL	0.18	0.09	0.09	0.10	0.91	0.20	0.53	0.72
DepthAnythingMetric	0.22	0.11	0.16	0.13	0.90	0.19	0.51	0.70

Table 7. Monocular depth estimator usage in our pipeline.

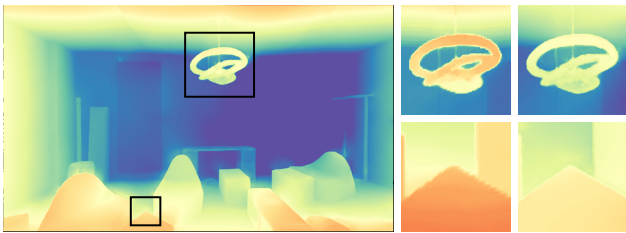


Figure 8. Refined edges through (u, v) coordinate refinement. Left crops: Initial depth map is exhibits jaggy edges along silhouettes. Right crops: After convergence, silhouettes are piece-wise linearly approximated by triangle edges.

Method	RMSE	MAE	L1-rel	L1-inv	δ_1	Acc. 0.01 m	Acc. 0.05 m	Acc. 0.10 m
Init Scale	0.17	0.11	0.09	0.10	0.93	0.10	0.41	0.65
After Local Ref.	0.16	0.09	0.07	0.10	0.93	0.21	0.58	0.76

Table 8. Depth map quality evaluated on our Scannet++ test scenes. Especially the accuracy metrics highlight the improvement gained through the local refinement (e.g. 110% improvement in case of $\tau=0.01$ m, while MAE was only lowered by $\approx 20\%$).

vancements in monocular estimators. Furthermore, although the Depth Anything Small (S) model produces results in seconds compared to minutes for Marigold, its performance is only marginally lower than its larger counterparts. Based on the overall slight lead, we chose Marigold as the default for our method.

Coordinate Refinement. Fig. 8 shows the influence of the (u, v) coordinate refinement, as introduced in Main-Sec. 3.7, thus counterbalancing the initial resolution loss by setting $d = 4$. This refinement significantly improved sharpness and accuracy in our depth maps, see Main-Tab. 3.

Intermediate Results. Tab. 8 shows the results after our initial global scaling and after the local refinement.

We can see great results, especially in the absolute, closeness based metric through our refinement strategies.